



Full Length Article

Transport studies in piezo-semiconductive ZnO nanotetrapod based electronic devices

Zhiwei Zhang^{a,b}, Morten Willatzen^{a,b,*}, Yogendra Kumar Mishra^c, Zhong Lin Wang^{a,b,d,e}

^a Beijing Institute of Nanoenergy and Nanosystems, Chinese Academy of Sciences, Beijing 101400, PR China

^b School of Nanoscience and Technology, University of Chinese Academy of Sciences, Beijing 100049, PR China

^c NanoSYD, Mads Clausen Institute, University of Southern Denmark, Alsion 2, DK-6400, Sønderborg, Denmark

^d CUSTech Institute, Wenzhou, Zhejiang, 325024, PR China

^e School of Materials Science and Engineering, Georgia Institute of Technology, Atlanta, Georgia 30332-0245, United States



ARTICLE INFO

Keywords:

ZnO nanotetrapods
Piezoelectric effect
Nano-piezoelectronics
Finite element method

ABSTRACT

ZnO nanotetrapods (ZnO NTs) with a non-centrosymmetric crystal structure consisting of four 1-D arms interconnected together through a central crystalline core, introduce interesting piezoelectric semiconducting responses in nanorods in the bent state. Considering the widespread applications of nanotetrapods in semiconductor devices, it becomes very crucial to establish a coupled model based on piezoelectric and piezotronic effects to investigate the carrier transport mechanism, which is being reported here in detail for the first time. In this work, we established a multiphysics coupled model of stress-regulated charge carrier transport by the finite element method (FEM), which considers the full account of the wurtzite (WZ) and zinc blende (ZB) regions as well as the spontaneous polarization dependence and the dependence of the material properties on the arm orientation. It is discovered that the forward gain of ZnO NT in the lateral force working mode is almost 50 % higher than that in the nanorod or in the normal force working mode while the reverse current is reduced to negligible. Through the simulation calculations and corresponding analysis, it is confirmed that the developed piezoelectric polarization charges are able to regulate the transport and distribution of carriers in ZnO crystal, which lays a theoretical foundation for the application of piezo-semiconductive ZnO NT devices in advanced technologies.

1. Introduction

Piezoelectric semiconductors, as an emerging electronic device, whose charge transport can be controlled by applying stress, hold a wide range of applications in sensors, actuators, and energy harvesting [1-7]. In recent years, the wurtzite piezoelectric semiconductor (also known as the third-generation semiconductor) materials, such as, ZnO, GaN, InN, and CdS, have received much attention due to the coupling of piezoelectric and semiconductor properties, among which, ZnO has become an interesting material due to its large number of nanostructural configurations [8-13]. A broad range of structural morphologies of ZnO material has been examined including nanowire [2], nanobelt [8], nanoring [14], nanohelix [15], nanotetrapod [16], etc., because of its distinctive crystallographic structure and alternating Zn²⁺ and O²⁻ polar surfaces [17]. The ZnO nanotetrapods (ZnO NTs) with three-dimensional (3-D) geometry, are one of these morphologies that

have garnered the most interest due to the unique structure in which two ZnO phases coexist: cubic and wurtzite, with an angle of about 109.5° between two adjacent arms [18,19]. Their unique 3-D morphology allows the excellent surface area accessibility of the individual arms regardless of their placement. Meanwhile, the greater stability is made possible by the simultaneous transfer of forces applied along one arm to the other arms [20]. Benefiting from this distinctive structure, especially the central core at the intersection of the four arms, the 3-D ZnO NTs differ significantly from conventional 1-D ZnO nanorods in terms of their mechanical, electrical, and semiconducting capabilities [18,20,21]. As a result, on the one hand, several studies have been done recently on the growth and fabrication of ZnO NTs, including thermal evaporation [22], chemical vapor deposition [23], vapor phase growth [24], and flame transport synthesis [25,26]. On the other hand, other communities has also documented significant applications of ZnO NTs in a variety of industries, including field-effect transistors (FETs) [19], force

* Corresponding author at: Beijing Institute of Nanoenergy and Nanosystems, Chinese Academy of Sciences, Beijing 101400, PR China.

E-mail address: mortenwillatzen@binn.cas.cn (M. Willatzen).

<https://doi.org/10.1016/j.mtelec.2024.100102>

Received 1 February 2024; Received in revised form 15 April 2024; Accepted 26 April 2024

Available online 30 April 2024

2772-9494/© 2024 The Author(s). Published by Elsevier Ltd. This is an open access article under the CC BY-NC license (<http://creativecommons.org/licenses/by-nc/4.0/>).

or gas sensors [27,28], ultraviolet (UV) detectors [29], supercapacitors [30], catalysis [31], which indicate that the ZnO NTs could be a potential choice for future applications related with piezoelectric semiconductor technologies [32-35].

Despite of their huge technological significance, most of the existing research on ZnO NTs focuses on synthesis and various applications. Some studies do mention the mechanical, electrical, and semiconducting properties of ZnO NTs, but there is still a lack of comprehensive theories and relevant models to explain the involved piezo related effects in detail to the best of our literature knowledge [36-38]. Since a nanotetrapod essentially consists of four nanorods, the ZnO NT already contains all the physical properties of the nanorod structure, which leads to a crucial realization—several methods for studying the piezoelectric properties of nanotetrapods may be directly adapted from 1-D nanorods [18,20,21]. The piezoelectric theory and continuum model were used to calculate the deformation and piezoelectric potential of 1-D ZnO nanorods. However, few researchers introduced doped carriers and discussed the effects of stress on carrier charge distribution and I-V curves [5, 39-41]. In order to apply the analytical method of nanorods to nanotetrapods, at least there are two open issues that need to be carefully addressed. First, previous studies on 1-D nanorods mostly utilize single semiconductor or piezoelectric models, which do not adequately capture the complete process of stress impacting carrier charge distribution and current output. In addition, the modeling of 1-D nanorods was mainly focusing on the P-N junction, while 3-D nanotetrapods, when used as semiconductor devices, control the carrier migration in the core region through stress, consequently generating an enhancement region and a depletion region, which is nearly identical to the model of field effect transistors.

In this work, based on piezoelectric and piezotronic effects, a multiphysics-coupled model of stress-regulated carrier transport in piezoelectric semiconductors is established. Extending this model from one-dimensional nanorods to three-dimensional nanotetrapods, the finite element method (FEM) is used to compute the piezoelectric potential and carrier concentration distribution in doped ZnO NTs. On this basis, we quantitatively calculated the impact of stress and doping concentration on the piezoelectric potential and carrier concentration and determined how these parameters affect the I-V curves by coupling with the semiconductor module. It is discovered that higher stress results in enhanced piezoelectric potential, stronger impact on carrier migration, and thus improved gains in forward amplification and reverse cut-off of the current. Specifically, under a tangential force of 1000 nN, the forward current has a gain close to 100 % while the reverse current is reduced to negligible. In addition, the increase in doping concentration will lead to an increase in the number of free carriers, which will significantly increase the current flowing through the ZnO NT while shielding the piezoelectric potential. Finally, the effect of stress direction on the current is discussed as well, and it is confirmed that the tangential stress along the direction of the source voltage has the best enhancement effect on the current, which demonstrates the superiority of ZnO NT as an advanced piezoelectric semiconductor sensor, because it can detect the magnitude and direction of stress simultaneously. Compared with 1-D ZnO nanorods of the same size and doping conditions, the ZnO NTs (in tangential force working mode) have about 50 % higher forward current gain amplitude while maintaining the base value of reverse current cut-off. Our presented model explains the mechanism of stress-regulated carrier transport and paves the way for understanding the piezoelectric semiconducting properties of ZnO NTs for a wide range of technological applications.

2. Results and discussion

2.1. Theoretical basis and research path

The ZnO material exhibits a non-centrosymmetric crystal structure and naturally generates a piezoelectric potential when subjected to an

external force. A typical ZnO NT structure, as shown in Fig. 1a, has a cubic zinc blende structure at the core, with four arms of a [0 0 0 1] wurtzite structure extending along $\langle 111 \rangle$ of the cubic structure, which results from the rapid growth of the wurtzite phase along the [0 0 0 1] polar axis. Taking the hexagonal wurtzite structure crystal as an example, the c-axis and the direction perpendicular to the c-axis clearly evidence an anisotropy. In a typical tetrahedral structure centered on Zn^{2+} cations and adjacent O^{2-} anions, the charge centers of cations and anions overlap when no external force acts. Once an external force is applied, the charge centers of cations and anions will shift relative to each other to generate a resultant non-zero dipole moment (Fig. 1a). The superposition of the dipole moments of all units in the crystal will generate a potential along the stress direction on the macroscopic scale, which is referred as the piezoelectric potential. The effect of applied stress on piezoelectric potential is also termed as piezoelectric effect.

The piezoelectric effect of ZnO also affects its carrier transport properties as a semiconductor. Fig. 1b shows the energy band diagram of the metal and free electron-doped ZnO (n-type semiconductor) in contact. If the work function of the metal material is greater than the electron affinity of the semiconductor material, a Schottky barrier ($e\Phi_{\text{SB}}$) will be formed at the contact interface between the metal and the semiconductor. Current can only flow through this barrier in one direction when the applied voltage is above this threshold. When ZnO is strained, the negative potential on the semiconductor side increases the height of the local Schottky barrier to $e\phi'$. Correspondingly, the positive voltage potential will lower the height of the Schottky barrier. The piezoelectric potential can be used to tune the carrier transport by changing the local barrier height, which is called piezotronic effect.

Our work focuses on the piezoelectric potential of ZnO nanotetrapods considering the free charge doping owing to the possible defects as well as the impact of the piezoelectric effect on the charge transfer of carriers because of their unique electromechanical properties among varieties of nanocrystalline structures. Fig. 1c shows our simulation model, consisting of a ZnO nanotetrapod placed on a plane that is fixed and grounded and is subjected to an external force. The external force can be either an axial traction/compression or a tangential stress that bends the nanotetrapod, under which ZnO NT will deform and a piezoelectric potential will be produced. By applying FEM, we use structural mechanics to calculate the deformation of the ZnO NT under force excitation, and couple structural mechanics and electrostatics through piezoelectric fields to obtain the distribution of piezoelectric potential in the nanotetrapod. In addition, the distribution of carrier concentration is altered by force, and the presence of free carriers has a substantial impact on the piezoelectric potential. To explore the distribution of piezoelectric potential with free carrier doping, simulations using the semiconductor module are required. Furthermore, an external circuit is used to measure the I-V characteristics of the ZnO NT, connecting the two arms of the ZnO NT to which electrical boundary conditions are applied. The whole simulation model includes four basic modules of structural mechanics, electrostatics, semiconductors, and circuits. The piezoelectric effect is used to couple structural mechanics and electrostatics, while structural mechanics and electrostatics are connected via charge and carrier distribution.

2.2. Piezoelectronic coupling model of a one-dimensional ZnO nanorod

In this section, we improved the piezoelectric model of one-dimensional ZnO nanorods, and for the first time established a multiphysics coupling model for stress-regulated carrier transport in piezoelectric semiconductors. To calculate the deformation and electric potential of ZnO, it is necessary to solve the static piezoelectric equation, including the mechanical equilibrium Eq. (1), the constitutive Eq. (2), and the electric Gaussian Eq. (3). When no physical force is added to the ZnO NT, the mechanical equilibrium equation becomes:

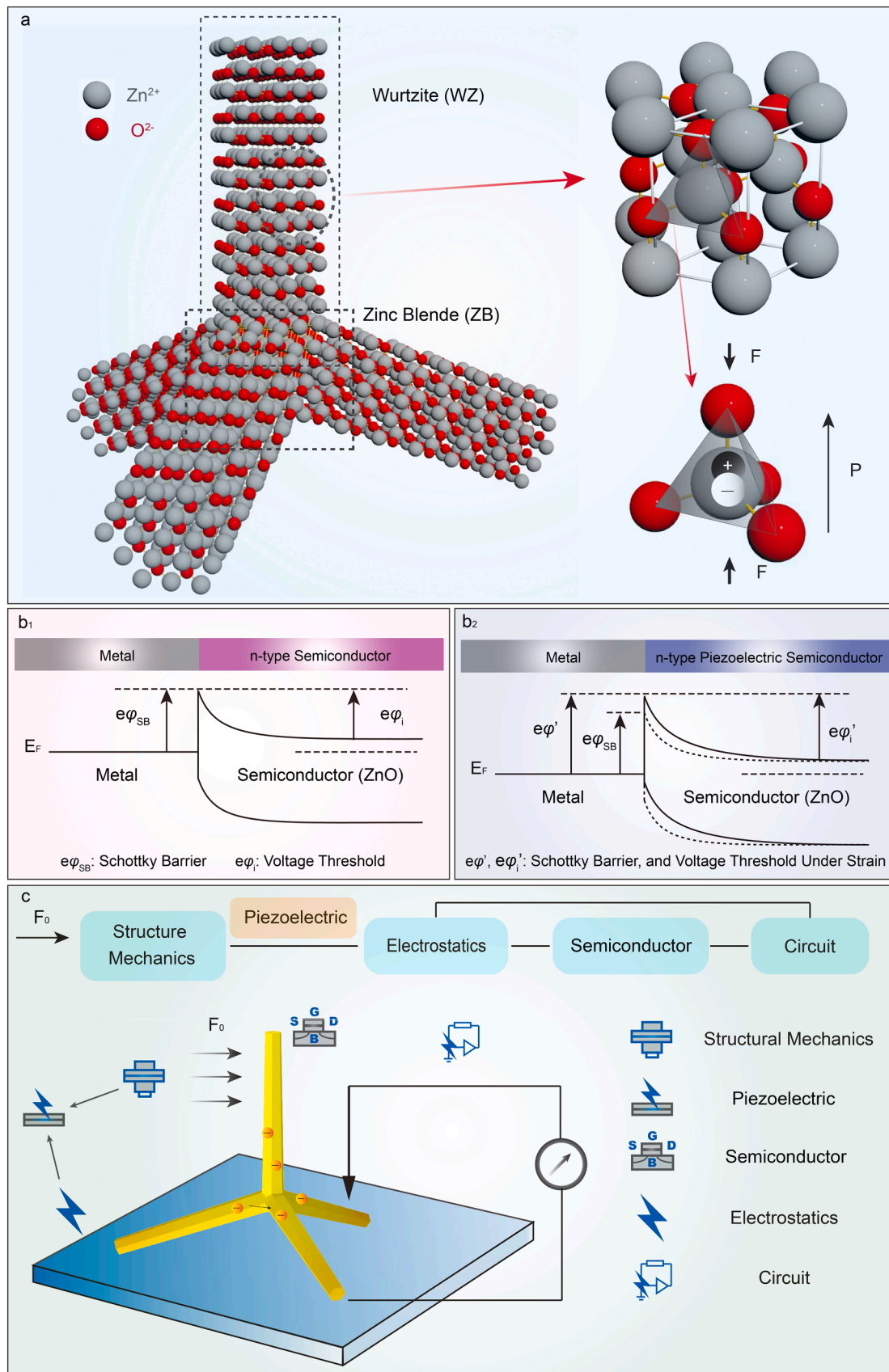


Fig. 1. ZnO Nanotetrapod Crystal Structure, Piezoelectric Properties, and Research Path.

a), Atomic structure of ZnO nanotetrapod crystal and piezoelectric effect under stress. b₁), Metal-Semiconductor Schottky contact energy bands, b₂), Metal-Semiconductor Schottky contact energy bands under piezoelectric electric fields. c), Numerical simulation path and physical field used in the finite element analysis method.

$$\nabla \cdot \mathbf{T} = \frac{\partial T_{ij}}{\partial x_j} = 0 \quad (1)$$

where \mathbf{T} is the stress tensor, which is related to strain ε , electric field \mathbf{E} , and electric displacement \mathbf{D} through the constitutive equation:

$$\begin{aligned} T_{ij} &= c_{ijkl}^E \varepsilon_{kl} - e_{kij} E_k \\ D_j &= e_{jkl} \varepsilon_{kl} + \kappa_{jk} E_k + P_j \end{aligned} \quad (2)$$

where c_{ijkl}^E is the stiffness tensor, e_{kij} , e_{jkl} means the piezoelectric tensor, and κ_{jk} represents the permittivity tensor. The parameters required for the simulation and the specific definitions of ZnO material tensors can be

found in Note. S1 and Note. S2. \mathbf{P} is the spontaneous polarization of wurtzite ZnO. Besides, assuming that no free charge ρ_e exists in ZnO NT, the Gaussian equation must be satisfied:

$$\nabla \cdot \mathbf{D} = \rho_e = 0 \quad (3)$$

Considering free carriers in the ZnO nanorod, the distribution of piezoelectric potential and carriers at thermal equilibrium needs to be reinvestigated. More exactly, the mechanical equilibrium equation and the constitutive equation continue to be the same as (1) and (2), while the charge density ρ_e is determined by the hole concentration p , electron concentration n , ionized donor concentration N_D^+ and ionized acceptor

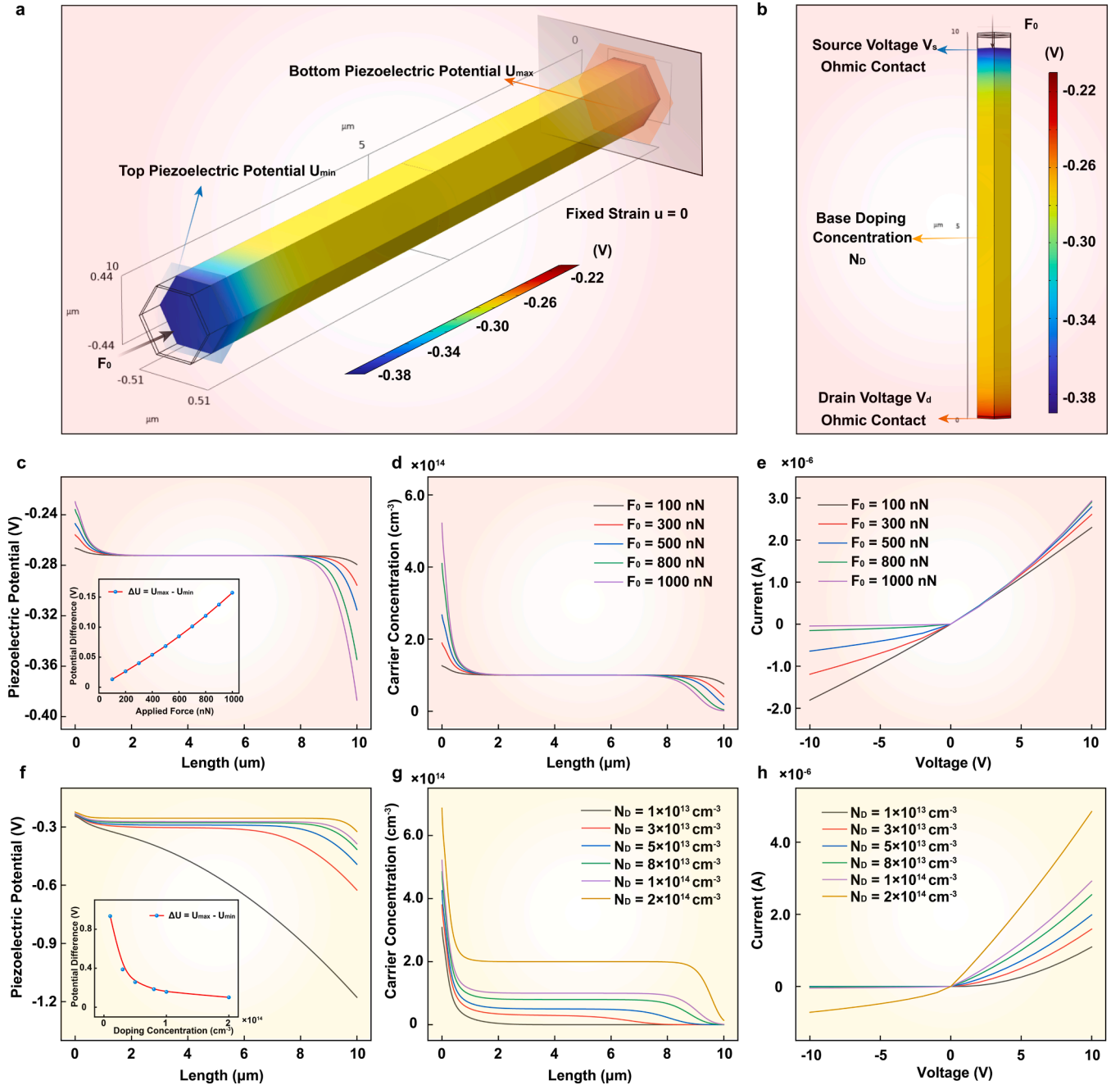


Fig. 2. Demonstration of a piezoelectronic coupling model of a one-dimensional ZnO nanorod

(a), Piezoelectric potential distribution and mechanical boundary conditions of carrier-doped ZnO nanorod. (b), Carrier doping and electrical boundary conditions (source voltage V_s and drain voltage V_d) of ZnO nanorod. (c), Piezoelectric potential distribution, and (d), Carrier concentration of ZnO nanorod under external force F_0 from 100 nN to 1000 nN. (e), I-V characteristic curve under the external force F_0 . (f), Piezoelectric potential distribution, and (g), Carrier concentration of ZnO nanorod with different doping concentration N_D from $1 \times 10^{13} \text{ cm}^{-3}$ to $2 \times 10^{14} \text{ cm}^{-3}$. (h), U-I characteristic curve with different doping concentration N_D .

concentration N_A^- , and the Gaussian equation for the electric field becomes:

$$\nabla \cdot \mathbf{D} = \rho_e = q(N_D^+ + p - N_A^- - n) \quad (4)$$

where q is the positive elementary charge. More detailed expressions for p , n , N_D^+ , and N_A^- can be found in Note. S2. Considering the n-type piezoelectric semiconductor, Gaussian Eq. (4) will become:

$$\nabla \cdot \mathbf{D} = \rho_e = q(N_D^+ - n) \quad (5)$$

The electric fields, charge densities, and currents are all correlated via current-density equations in the following way:

$$\begin{aligned} \mathbf{J}_n &= q\mu_n n \mathbf{E} + qD_n \nabla n \\ \mathbf{J}_p &= q\mu_p p \mathbf{E} + qD_p \nabla p \end{aligned} \quad (6)$$

where \mathbf{J}_n and \mathbf{J}_p are the electron and hole current densities, μ_n and μ_p are the electron and hole mobilities, D_n and D_p are the diffusion coefficients for electrons and holes, \mathbf{E} is the electric field.

In addition, the continuity equations are utilized to describe the charge transport driven by the electric field:

$$\begin{aligned} \frac{\partial n}{\partial t} &= G_n - U_n + \frac{1}{q} \nabla \cdot \mathbf{J}_n \\ \frac{\partial p}{\partial t} &= G_p - U_p + \frac{1}{q} \nabla \cdot \mathbf{J}_p \end{aligned} \quad (7)$$

where G_n and G_p are the electron and hole generation rates, U_n and U_p are the recombination rates, respectively. Eqs. (2), (4), (6), and (7) form the basis for solving the multiphysics-coupled ZnO piezoelectric semiconductor model together.

Fig. 2a shows our model and mechanical boundary conditions of 1-D ZnO nanorods. The uniform nanorod with a hexagonal cross-section is fixed at one end, and a compressive force of 1000 nN along the axial direction of the nanorod is applied at the other end. It should be noted that this model takes into account the effect of doping carrier charges. At the doping concentration of 10^{14} cm^{-3} , the potential distribution of ZnO nanorod is also shown in Fig. 2a. Compared with undoped nanorods (Fig. S2), there is a significant drop in potential due to the shielding effect of doped charges, which was also reported in previous studies [6, 40]. Specifically, the potential of the wide central region of the ZnO nanorod remains unchanged but the potential at both ends increases or decreases significantly. This is because the doped carriers currently dominate the piezoelectric potential, and the carrier charges accumulate/deplete at two ends of the ZnO nanorods under pressure, which leads to a significant change in the carrier concentration at the ends of the arms while remaining stable in the middle. Additionally, the total potential is negative since this model applies n-type doping. Fig. 2c and Fig. S3 further demonstrate the effect of pressure F_0 on the piezoelectric potential. It is discovered that the greater the pressure F_0 , the more significant the potential drop on both sides. Note that the maximum potential at the fixed end is U_{\max} , the minimum potential at the force-applying end is U_{\min} , and the potential difference is defined as $\Delta U = U_{\max} - U_{\min}$, which will increase significantly with the increase of pressure F_0 . Since as F_0 increases, the accumulation/depletion of carrier charges on both sides will be more significant, as shown in Fig. 2d. Besides, the effect of the doping concentration N_D on the piezoelectric potential is also analyzed. The greater the doping carrier concentration N_D , the more obvious the shielding effect of free carriers on the piezoelectric field, and thus the smaller the potential drop at both ends of the nanorod (Fig. 2f). When the doping concentration N_D decreases to 10^{13} cm^{-3} , the potential distribution is similar to the linear decrease without carrier doping. On the contrary, if the doping concentration is increased to 10^{14} cm^{-3} , there will be two non-negligible voltage drop regions on both sides of each arm while the potential of the middle part will hardly change. Similar circumstances also apply to the carrier distribution, where both ends will more visibly demonstrate the accumulation or

depletion of carrier charge with increasing doping concentration N_D , while the center remains at the base doping concentration (Fig. 2g).

On this basis, the properties of ZnO nanorods as piezoelectric semiconductors are considered. The electrical boundary conditions are set as shown in Fig. 2b. The fixed end of the nanorod is used as the drain, whose voltage is set to 0, while the force-bearing end is set as the source, whose voltage is set to V_s . Both ends are in ohmic contact with the electrodes. In general, the current flowing through the ZnO nanorod shows positive enhancement and negative inhibition, which means that when the source-drain potential difference is positive, the current increases compared to when no pressure is applied, and vice versa. This is because the potential barrier at the force-applying end (source) will be significantly increased and the potential barrier at the fixed end (drain) will be lowered after the compressive external force is applied to the ZnO piezoelectric semiconductor. The greater the applied external force, the greater the effect on the potential barrier, so the forward current is larger and the reverse current is smaller, as shown in Fig. 2e. Fig. S4 demonstrates in more detail the variation of the drain barrier under a gradually increasing external force F_0 . As F_0 increases from 100 nN to 1000 nN, the height of the potential barrier also rises from $e\phi_1$ to $e\phi_5$, so it will be more difficult for carriers to pass through, showing the reverse cut-off of current. Besides, Fig. 2h also illustrates the influence of doping concentration on current, from which it can be observed that the higher the doping concentration, the greater the current in both forward and reverse directions. The increase in doping concentration will increase the number of free carriers, so there is a gain effect on both forward and reverse currents. In the above discussion, the contacts between the ZnO nanorod and metal electrodes are all set as ohmic contacts. Fig. S5 supplements and compares the influence of ohmic contact and Schottky contact on the current. A perfect Schottky contact (in the absence of piezoelectricity) can make the reverse current close to zero while the forward current is unaffected (Fig. S5b). When the external force is small ($F_0 = 100 \text{ nN}$), the U-I curve is close to the ideal ohmic contact, and when increasing F_0 to 1000 nN, the effect of approximate Schottky contact can be achieved (Fig. S5c). In summary, this section establishes a coupled model of the ZnO piezoelectric semiconductor and verifies it in the 1-D nanorod. The impact of doping carrier charges on the piezoelectric potential is investigated, and the relationship between the doping concentration and the current flowing through the nanorods is further analyzed.

2.3. Piezoelectronic properties of a ZnO nanotetrapod

In the previous section, a multiphysics-coupled piezoelectric semiconductor model of a one-dimensional ZnO nanorod is proposed. This method can be extended from one-dimensional to three-dimensional and a ZnO nanotetrapod model with doped carriers is established. As shown in Fig. 3a and Fig. S6, the ZnO NT is placed on a plane with the bottom fixed, which means that the part in contact with the plane satisfies $u_z = 0$. Meanwhile, a pressure of F_0 is applied on top of the ZnO NT along the normal direction of the plane and the base doping concentration of the whole structure is N_D . Under this boundary and excitation condition, the deformation and piezoelectric potential distribution of ZnO NT are shown in Fig. 3a. The bottom three arms bend down under the force, and the maximum displacement is around 18 nm. The piezoelectric potential cross-sections on the XY, YZ, and ZX planes are selected for display. To identify the distribution of the piezoelectric potential more clearly, the potential stubs along the L and -L directions are chosen to show. It is worth noting that only one of the bottom three arms is selected as a representative because the displacement and potential distribution of the bottom three arms are symmetrical and consistent. The potential distribution of ZnO NT under the influence of doped carriers inherits some properties of the nanorod, such as keeping the potential substantially constant in the middle of each arm and having abrupt changes at both ends. The difference lies in the core region where the four arms intersect, where the potential is the result of

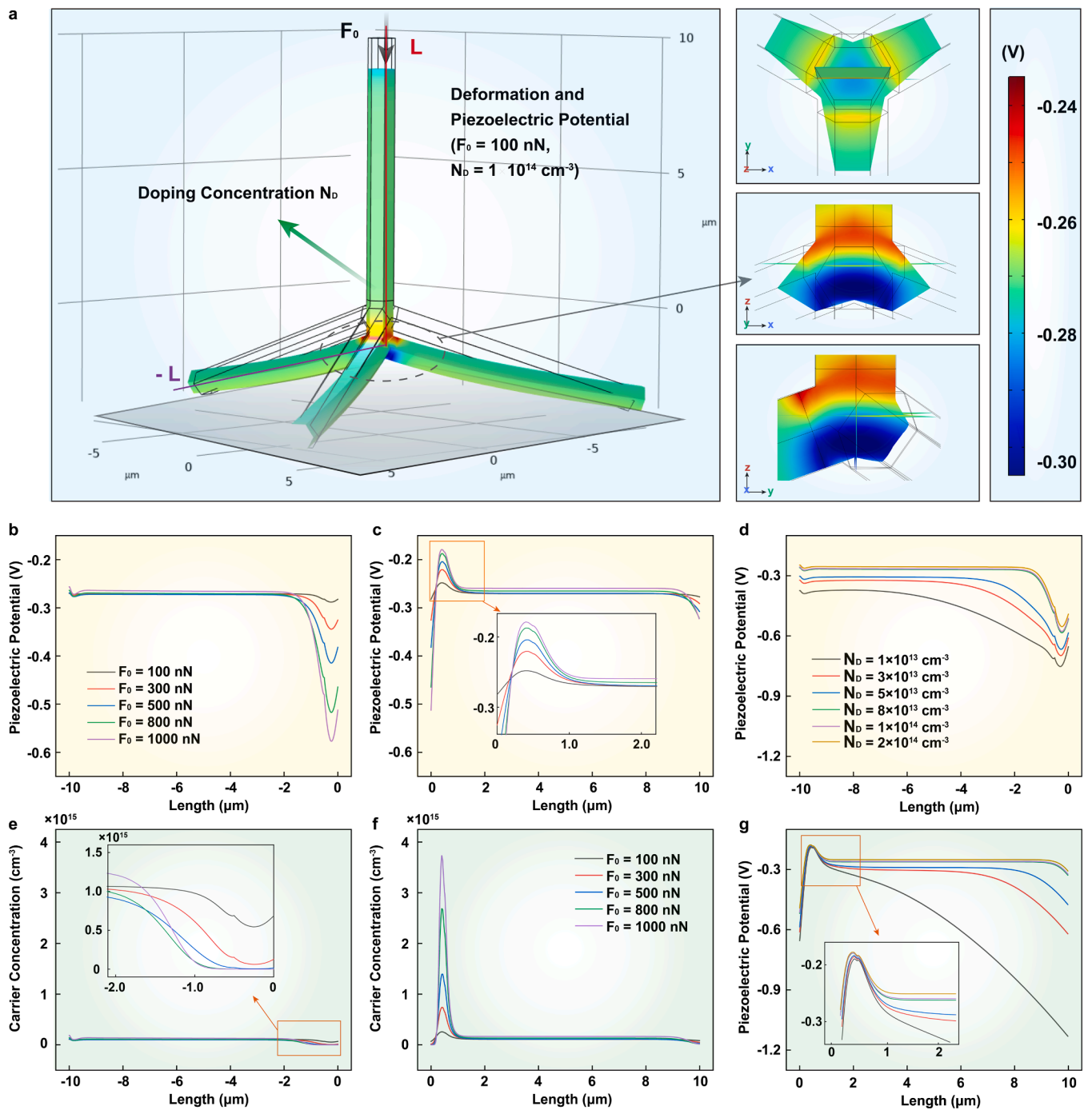


Fig. 3. Piezoelectric properties of a ZnO nanotetrapod under normal force

a), Piezoelectric potential and 3-D section distribution of carrier-doped ZnO nanotetrapod under normal force $F_0 = 100$ nN. b), Piezoelectric potential along the - L direction and c), + L direction under normal force F_0 from 100 nN to 1000 nN. d), Piezoelectric potential along the - L direction with different doping concentration N_D from $1 \times 10^{13} \text{ cm}^{-3}$ to $2 \times 10^{14} \text{ cm}^{-3}$. e), Carrier concentration along the - L direction and f), + L direction under normal force F_0 from 100 nN to 1000 nN. g), Piezoelectric potential along the + L direction with different doping concentration N_D from $1 \times 10^{13} \text{ cm}^{-3}$ to $2 \times 10^{14} \text{ cm}^{-3}$.

the comprehensive action of the four arms. Due to the continuity of the potential, there will be a transitional change in this region from the potential minimum of the bottom arm to the potential maximum of the top arm. Therefore, the core region is very sensitive to external forces and changes in doping concentration. As shown in Fig. 3b and Fig. 3c, the effect of force F_0 on ZnO NT piezoelectric potential is similar to that of nanorod, more specifically, the generated piezoelectric potential increases with increasing axial force. The reason is also closely related to the distribution of carriers, that is, the larger the F_0 , the more carrier

charges are accumulated/depleted at the ends of the four arms of the ZnO NT and the core region (Fig. 3e and Fig. 3f). For example, electrons will deplete more in the core area (coordinate origin) with the increase in the force F_0 . When the force F_0 increases, the potential of the core area also decreases. As for the doping concentration, which is shown in Fig. 3d and Fig. 3g, the greater the concentration of doped carriers, the more obvious the shielding of the piezoelectric field due to free carriers, and thus the smaller the potential along the -L to L direction. When the doping concentration is 10^{13} cm^{-3} , the piezoelectric potential

distribution is similar to that without doping, and when it increases to 10^{14} cm^{-3} , each arm will have a distribution with no change in the middle and sudden changes at both ends (Fig. S7). It is worth mentioning that both the type of doping (n-type/p-type) and the type of force (compression/traction) affect the distribution of the piezoelectric potential, which has been reported in 1-D nanorod [6]. All of these findings demonstrate that the piezoelectric potential of nanorods with n-type and p-type doping, or under compression and traction has symmetry, which extends to the piezoelectric potential of ZnO NT, which can be seen in Fig. S8 and Fig. S9. The potential distribution of n-type doping is consistent with that of p-type doping under a doping concentration of 10^{14} cm^{-3} and a force of 1000 nN, but the positive and negative are the reverse. More specifically, the potential distribution of n-type doped ZnO NT under compression is similar to that of p-type doped ZnO NT under traction, and vice versa. In conclusion, under the action of normal force, the carrier doping will shield the piezoelectric potential, which will be strengthened with the increase of doping concentration.

The piezoelectric potential distribution of the ZnO NT under normal external force and the influence of different forces and doping concentrations have been discussed. However, in experiments and applications, the external force may also come from the tangential direction in addition to the normal direction. Since the tangential force will cause the ZnO NT to slide on the plane, the part where it meets the plane is completely fixed, that is, $u = 0$, and the rest of the conditions are the same as those under the normal force. Under the influence of tangential force, the ZnO NTs can deform up to 90 nm, as shown in Fig. S10a. The region with the largest piezoelectric potential difference occurs at the junctional core region of the tetrapod, with relatively positive piezoelectric potential on the compression side and negative piezoelectric potential on the stretching side. The cross-sections on the XY, YZ, and ZX planes show the piezoelectric potential distribution in the core region in detail. Take the potential stubs along the four arms of ZnO NT, denoted as $L_1 \sim L_4$, and the more intuitive potential distribution is shown in Fig. S10b. Due to the tangential force's influence, there is also compression in the L_1 direction, which leads to a potential drop close to the core, which is comparable to the performance when an external force is applied in the normal direction. L_3 and L_4 are symmetrical and also show consistency in potential distribution. The overall piezoelectric potential is negative because of the n-type doping. If the center point of the intersection of $L_1 \sim L_4$ is used as zero potential references, a relatively positive potential will appear on the bending side of the ZnO NT, and a negative potential will appear on the opposite side, which is similar to the potential distribution of a bent 1-D nanorod [42]. In addition, at the position far from the core region, the piezoelectric potentials in the directions of the four arms are the same. The distribution of carriers is similar to the potential, which is shown in Fig. S10e. The rule that the piezoelectric potential is affected by the tangential force is consistent with the normal force, that is, a greater force can produce a larger piezoelectric potential, as shown in Fig. S10c and Fig. S10d. Here, the piezoelectric potential distribution along the L_2 and L_3 directions of the tangential force is taken as a representative (The piezoelectric potential and carrier concentration distribution in the L_1 direction can be found in Fig. S11). This can also be attributed to the pressure regulation of carrier charge transport, with higher pressure causing more carrier charge accumulation at the bent end and depletion at the opposite side (Fig. S12). The effect of doping concentration is shown in Fig. S10f and Fig. S10g. The increase in doping concentration will make it easier for carriers to gather in the core region, thus increasing the strength of the concentration/depletion region. In addition, the direction of the force F_0 also affects the calculation results. Fig. S13 - Fig. S15 shows the distribution of piezoelectric potential and carriers under the action of tangential force in the opposite direction. It is predictable that based on the symmetry the distribution of the piezoelectric potential and carrier concentration is similar but in opposite directions. Through the calculation of ZnO NT under carrier doping, it is discovered that the piezoelectric potential of ZnO NT is influenced by the doping carrier

concentration and the normal/tangential force also affects the distribution of the carrier concentration, which provides a crucial method to modulate the piezoelectric potential by the doping concentration or to adjust the carrier transport by altering the stress.

2.4. UI characteristics of a ZnO nanotetrapod semiconductor

The previous section briefly described the principle of regulating the piezoelectric potential by changing the doping carrier concentration and found that the carriers in ZnO NT can be controlled by the piezoelectric effect. In fact, some studies have exploited this property of ZnO NT to fabricate novel piezoelectric semiconductors [27]. In this section, the principle of piezoelectrically regulated ZnO NT will be explained, and the theory will be verified by simulation models. We calculated the semiconductor properties of the ZnO NT as a field effect transistor in the two working modes of normal force and lateral force mentioned in the last chapter. The basic model for the working mode under normal force remains unchanged, that is, the ZnO NT with a base doping concentration of N_D (or N_A if the ZnO NT is p-type doping) is placed on a fixed plane, which means $u_z = 0$, and a compression or traction force of magnitude F_0 is applied on the top along the normal direction. The difference is the electrical boundary conditions. The L_1 terminal is used as the source and the L_2 terminal is used as the drain to be grounded, while the carrier transport is controlled by the compression or traction force exerted by the L_1 terminal. According to the conclusion of the previous section, under the compressive force, carriers in the L_1 direction will flow into the core region from the top, thus forming a depletion region at the top and an accumulation region in the core area. Meanwhile, fewer carriers in the $L_2 - L_4$ direction will also migrate to the core area. The compressive force reduces the height of the potential barrier, causing an increase in the forward current, while exhibiting a hindering effect on the reverse current, which can be seen in Fig. S16. Fig. 4b and Fig. 4c discuss the impact of the compressive external force and doping concentration on the current. The greater the compressive force, the wider the accumulation/depletion region of ZnO NT, so the forward current is larger and the reverse current is smaller. Besides, the increase in doping concentration will increase the number of carrier charges, thereby showing a gain for both forward and reverse currents. Compared with nanorod, ZnO NT has a similar gain effect on forward current (about 50 %) in the normal force operating mode, and the reverse current can also be almost completely eliminated. On the contrary, if a traction force is applied (Fig. 4d), the carriers are depleted in the core region and accumulated at the top, thus showing obstruction to the forward current and enhancement of the reverse current. Fig. 4e - Fig. 4g further supplement the I-V curve of p-type doping, whose conclusion still shows good symmetry. In other words, the potential distribution of n-type doped ZnO NTs under compression is similar to that of p-type doped ZnO NTs under traction, and vice versa. As described already, changing the external force and doping concentration under p-type doping is consistent with the rules in the case of n-type doping.

For the working mode under tangential force, the potential V_g is applied to the L_2 terminal as the source, the L_3 terminal is used as the drain to be grounded, and the L_1 is used as the gate to adjust the size of the depletion layer, which constitutes a simple field effect transistor, as shown in Fig. 5a. The most crucial part in the entire structure is the L_1 terminal as the gate, which will bend down under the action of the external force F_0 , causing the carriers in the directions of L_1 and L_3 to flow into L_2 . Thus, an accumulation region is formed on the bending side of the core region and a depletion region on the opposite side. The energy level distribution of this accumulation/depletion region is shown in Fig. S17. For forward current, the bending caused by the external force will reduce the height of the barrier and thus play a gain effect. On the contrary, for the reverse current, the potential barrier will be raised to show the characteristics of the reverse cut-off. Fig. 5b compares the current output characteristics of piezoelectric and non-piezoelectric

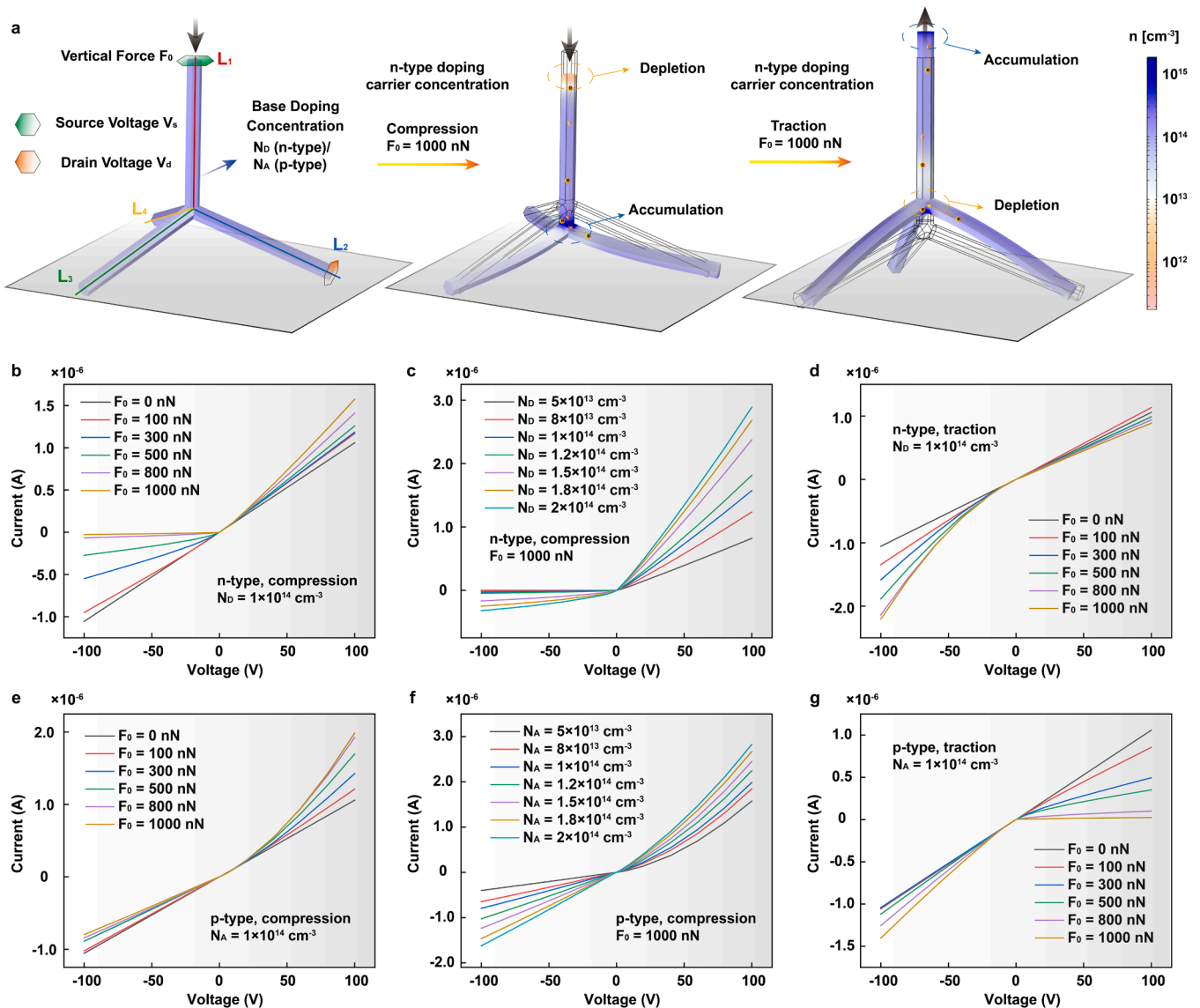


Fig. 4. Semiconductor properties and I-V characteristic curves of a ZnO nanotetrapod under normal force

a) Schematic diagram of carrier distribution and migration of ZnO nanotetrapods under compressive or tensile force F_0 . b), I-V curves under compressive force F_0 from 0 to 1000 nN (n-type doping, $N_D = 1 \times 10^{14} \text{ cm}^{-3}$). c), I-V curves with different doping concentration N_D from $1 \times 10^{13} \text{ cm}^{-3}$ to $2 \times 10^{14} \text{ cm}^{-3}$ (Compressive force, $F_0 = 1000 \text{ nN}$). d), I-V curves under tensile force F_0 from 0 to 1000 nN (n-type doping, $N_D = 1 \times 10^{14} \text{ cm}^{-3}$). e), I-V curves under compressive force F_0 from 0 to 1000 nN (p-type doping, $N_A = 1 \times 10^{14} \text{ cm}^{-3}$). f), I-V curves with different doping concentration N_A from $1 \times 10^{13} \text{ cm}^{-3}$ to $2 \times 10^{14} \text{ cm}^{-3}$ (Compressive force, $F_0 = 1000 \text{ nN}$). g), I-V curves under tensile force F_0 from 0 to 1000 nN (p-type doping, $N_A = 1 \times 10^{14} \text{ cm}^{-3}$).

materials. It can be observed that the I-V curves of non-piezoelectric materials are completely linear, while piezoelectric materials show an increase in forward current and a suppression of reverse current under pressure. In addition, the contact with the electrodes is also considered. As we know, the contact between metal and semiconductor forms a potential barrier, and only a source voltage above the barrier can generate current. Fig. 5c shows the I-V curve after replacing the source with a Schottky contact. It is discovered that ZnO semiconductors under piezoelectric control can achieve similar results to Schottky contacts under the condition of ohmic contacts, so the role of electrode contacts in the calculation can be ignored. Besides, Fig. S18 compares the output curves of ZnO NT under the normal force and tangential force. It can be clearly observed that when the magnitude of force is constant, the gain effect of the tangential force on the forward current is more obvious, while the cut-off effect on the reverse current shows no significant difference. More specifically, the forward gain of ZnO NT in the lateral force working mode is about 50 % higher than that in the nanorod and

normal force working mode. Furthermore, we proceed to discuss the effects of force and doping concentration on the current through ZnO NTs. From Fig. 5d, it can be found that a larger F_0 will make the accumulation/depletion region of the core region wider and the ability to control carrier transport is also stronger, leading to a higher forward current and a lower reverse current. The I-V curves and structure of ZnO nanotetrapod logic devices are displayed in Fig. S19 and Fig. S20. Similar findings to those of our simulation model—reverse cutoff and forward enhancement—are evident [17,27]. The forward current increases with the degree of bending, and reverse bending causes the current to flow in the opposite direction. As for the doping concentration, the effect is similar to that of the 1-D nanorod, which means that the number of base carrier charges will rise with an increase in doping concentration, having a gain impact on both forward and reverse currents.

Furthermore, we investigated how the size of the ZnO NT affected the I-V curve (Fig. S21). We define the height of a single nanorod is h

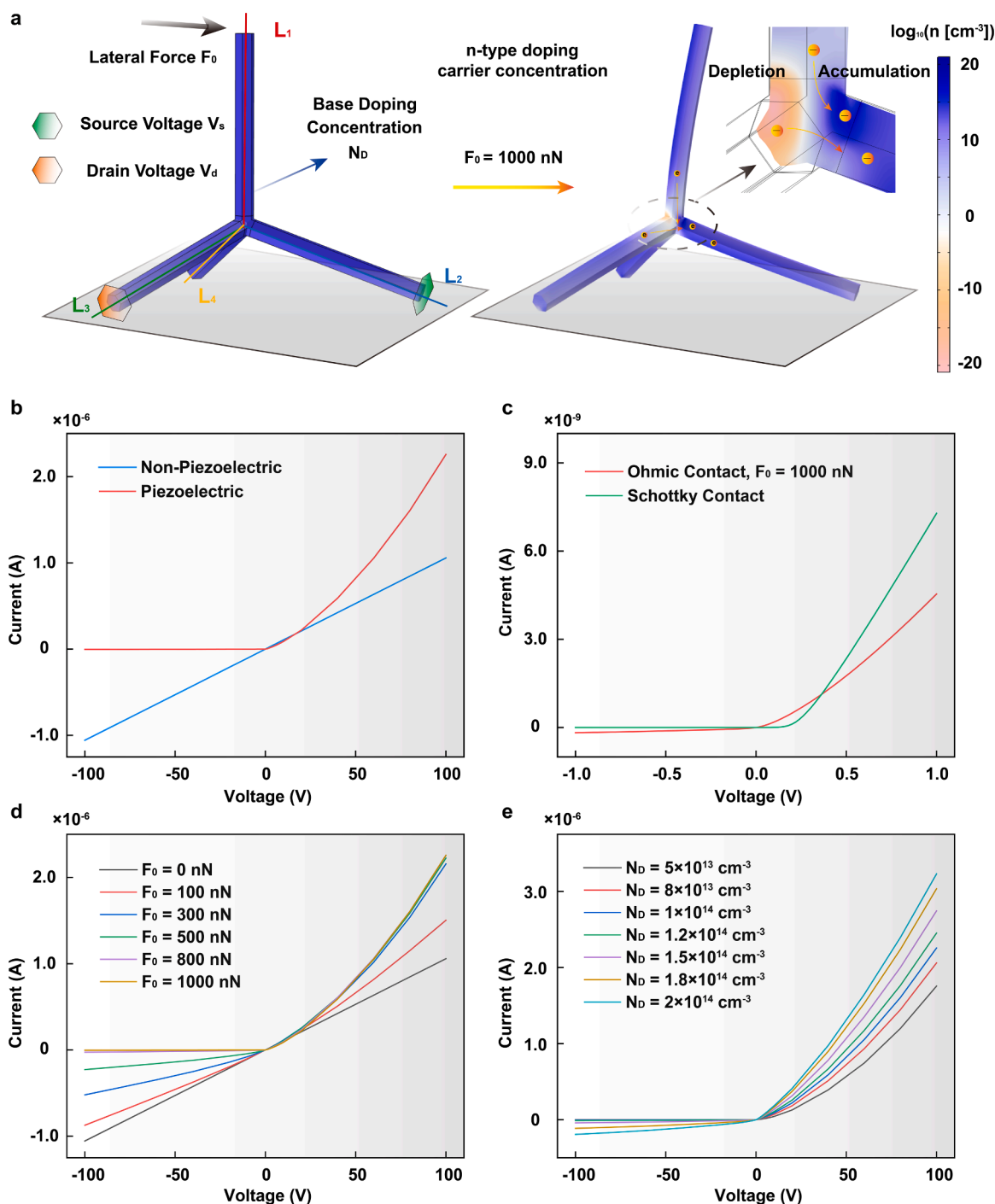


Fig. 5. Semiconductor properties and I-V characteristic curves of a ZnO nanotetrapod under horizontal force.

a), Schematic diagram of carrier distribution and migration of ZnO nanotetrapods before and after horizontal force F_0 . b), Comparison of I-V curves of piezoelectric materials and non-piezoelectric materials. c), Comparison of I-V curves with Ohmic Contact under applied force $F_0 = 1000$ nN and Schottky Contact. d), I-V curves under tangential force F_0 from 0 to 1000 nN. e), I-V curves with different doping concentration N_D from 1×10^{13} cm $^{-3}$ to 2×10^{14} cm $^{-3}$.

(the four legs that make up the ZnO NT are of the same size, and changing the shapes works for all four legs.), the edge length of the top regular hexahedron is l_1 , and the bottom edge length is l_2 . When the upper and lower side lengths of the nanorods are the same, we define $l = l_1 = l_2$, and when they are different, the length ratio $r = l_2/l_1$ is used to describe its shape. The model and boundary condition settings are shown in Fig. S21a. We still set one arm as the source and the other as the drain, and apply a tangential force of 1000 nN on the top as gate control. We find that when the height of a single nanorod composing ZnO NT increases from $2 \mu\text{m}$ to $10 \mu\text{m}$, the forward current via ZnO NT

will first increase and then drop, and the current will reach its maximum when $h = 4 \mu\text{m}$ (Fig. S21b, Fig. S21e). As the length or side length ratio of a single nanorod increases (l : 0.4 μm to 0.6 μm , r : 1.0 to 3.0), the forward current will keep rising (Fig. S21c, Fig. S21d, Fig. S21e, Fig. S21f), while the reverse current has the same rules as the forward current, but the amplitude will be reduced by more than a hundred times (Fig. S22), which means that the change in reverse current with size is negligible. Overall, in this chapter, we tuned the carrier transport properties through the piezoelectric effect and finally built a model to realize the role of ZnO NT as fundamental FET.

2.5. Effect of stress direction on a ZnO nanotetrapod semiconductor

In addition to the magnitude of the force, the direction will also affect the distribution of the carrier charge and thus control the output current. Fig. S10 and Fig. S13 show the difference in piezoelectric potential and carrier distribution caused by external forces in opposite directions. In this section, we discussed in more detail how the direction of force affects current. Note that the direction opposite to the source (L_2 direction) is the 0-degree line, and the angle formed by the tangential force and the 0-degree line is the direction of angle (DOA), as shown in Fig. 6a. Fig. 6b shows the carrier concentration distribution along the drain to the source under an external force of $F_0 = 1000$ nN and an azimuth angle from 60° to 240° (based on symmetry). In general, the carrier concentration on one side that is consistent with the direction of the force increases, while the carrier concentration on the other side decreases, and when $DOA = 180^\circ$, the concentration difference is most obvious. Fig. 6c shows how the current varies with the source-drain voltage from 0° to 300° . When $DOA = 180^\circ$, the forward current is the largest and the reverse current is almost 0, while the situation is completely opposite when $DOA = 300^\circ$. The former bends the gate toward the source, while the latter bends toward the drain. The accumulation/depletion layers of the two are just opposite, and such a result is also expected. In addition, the I-V curve is just a straight line when $DOA = 60^\circ$, because the force just does not point to either the source or the drain. Fig. 6d and Fig. 6h comprehensively demonstrate the changes in current with DOA at source voltage $V_s = 1$ V and $V_s = -1$ V, respectively, confirming our previous conclusion that $DOA = 180^\circ$ and 300° correspond to the positions with maximum forward current and maximum reverse current. To describe the effect of DOA on the current better, we take $I_{sum} = I(V_s = 1\text{ V}) + I(V_s = -1\text{ V})$, and the result is shown in Fig. 6f. When $I(V_s = 1\text{ V}) > I(V_s = -1\text{ V})$, I_{sum} is positive, otherwise it is negative. The larger the absolute value of I_{sum} , the more significant the

gain on the forward current and the cut-off effect on the reverse current. The smaller the I_{sum} , the less likely it is to enhance the forward and weaken reverse currents. Specifically, $I_{sum} = 0$ means that the current is neither enhanced nor weakened under this DOA. Fig. 6f presents a fairly symmetrical "butterfly" pattern with $DOA = 60^\circ$ and $DOA = 240^\circ$ as the axes of symmetry. All of the above indicates that when the gate of ZnO NT is bent to the source, the gain to the forward current is the largest, and the resistance to the reverse current is the most significant. Conversely, if it is bent towards the drain, the reverse current can be increased to the greatest extent and the forward current can be suppressed. Bending towards the fourth arm, which does not belong to either port, gives no gain or weakening, and exhibits complete symmetry with that direction as the axis of symmetry.

3. Conclusion

In summary, a multiphysics-coupled model of stress-regulated carrier transport is established via the finite element method (FEM), and the working principle of ZnO nanotetrapod as piezoelectric semiconductor is elucidated, based on which we further discussed the influence factors of current output. It is demonstrated that stress leads to the depletion and accumulation of carrier charges through the piezoelectric effect at the compressive end and the fixed end of the ZnO nanoarms, respectively. Carrier charges which migrate due to stress cause a redistribution of the piezoelectric potential, exhibiting abrupt changes at the two ends and relative constancy in the middle. The redistribution of carrier charges will also reduce the potential barrier of the source and increase the barrier of the drain, thereby increasing the forward current and hindering the reverse current, which is also the working mechanism of the ZnO nanorod as a semiconductor. For the one-dimensional ZnO nanorod, the forward current is amplified by approximately 50 % under the action of an external force of 1000 nN, while the reverse current will

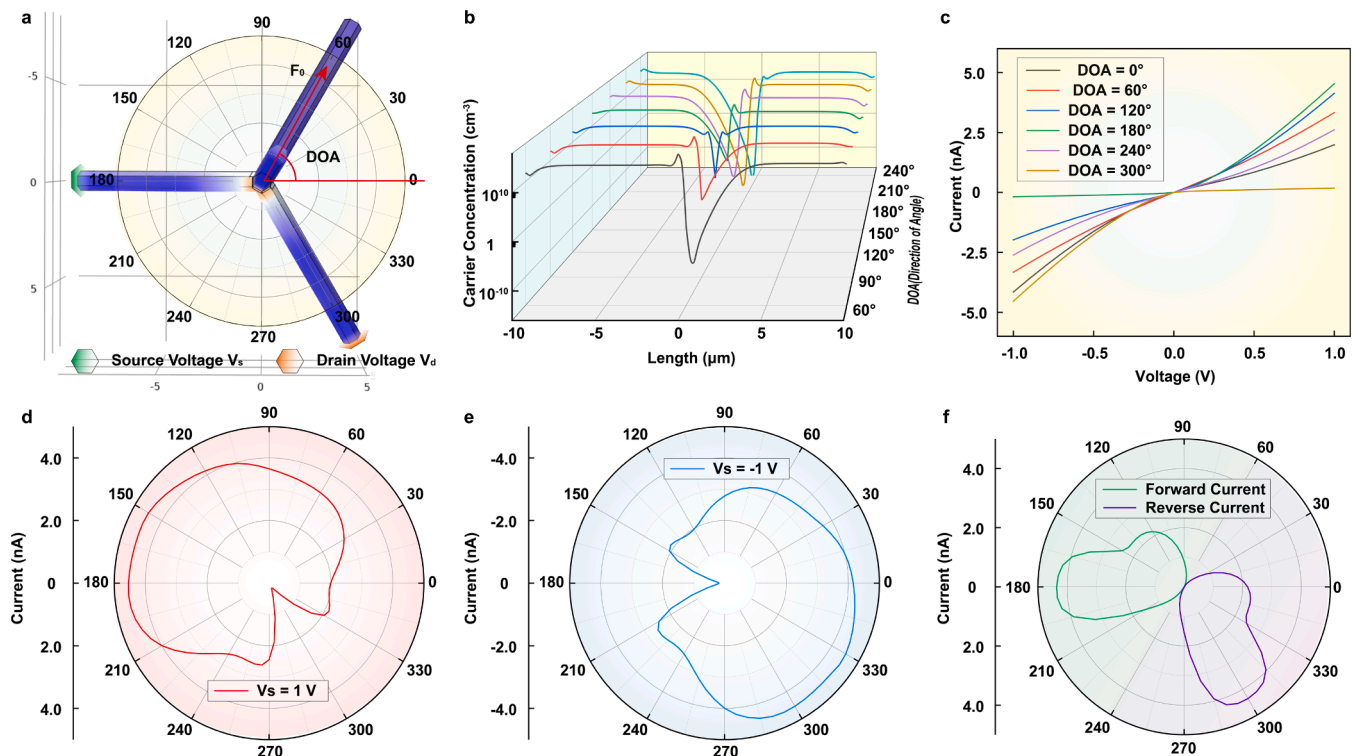


Fig. 6. Effect of stress DOA on ZnO nanotetrapod semiconductor

a), Schematic diagram of the direction of the tangential force, i.e. the direction of angle (DOA). b), Carrier concentration under the tangential force with different DOA. c), I-V curves with different DOA from 0° to 300° d), Radar diagram of the current under different angles of tangential force when the gate voltage $V_s = 1$ V. e), Radar diagram of the current under different angles of tangential force when the gate voltage $V_s = -1$ V. f), Radar diagram the sum of current ($I(V_s = 1\text{ V}) + I(V_s = -1\text{ V})$).

reduce to almost zero.

The present multiphysics-coupled piezoelectric semiconductor model is first applied to 1-D nanorods and then extended to 3-D nanotetrapods. It is demonstrated that the same shielding effect observed for ZnO nanorods also exists in ZnO NTs, and the shielding effect becomes more significant with the increase of doping concentration. We determined the piezoelectric potential and carrier distribution of ZnO NT subject to normal and tangential forces and reported that both the sudden change of piezoelectric potential and the accumulation and depletion of carriers occur in the central crystalline core where the nanoarms intersect. In the normal force working mode, the gain effect of ZnO NT on forward current is similar to that of the nanorod (about 50 % gain), and the reverse current can also be almost completely eliminated.

This finding indicates that ZnO NT can be used as a new type of semiconductor element for advanced FET devices. Using the vertical arm of the ZnO NT as the gate and any two arms at the bottom as the source and drain, a basic FET model is constructed. The size and strength of the depletion layer in the core region of the ZnO NT can be effectively changed by altering the applied force on the top, and its I-V curve exhibits the characteristics of forward enhancement and reverses cut-off, indicating the application feasibility of nanotetrapods in FET device. In the lateral force working mode, the forward gain of ZnO NT is about 50 % higher than that in the nanorod and normal force working mode, and the reverse suppression effect remains almost unchanged. Finally, the presented DOA analysis shows that a tangential force along the source direction results in the largest forward current gain and the highest reverse current suppression. The results also demonstrate ZnO NT's supremacy as a piezoelectric semiconductor sensor—that is, its simultaneous detection of stress direction and magnitude. The efforts we made in this work not only represent a reference study for the preparation of ZnO NTs with excellent piezoelectric and piezotronic properties but also provide a pathway for a deeper understanding of the electromechanical carrier transport properties of ZnO NTs as a new generation of piezoelectric semiconductors.

CRedit authorship contribution statement

Zhiwei Zhang: Writing – original draft, Software, Investigation, Formal analysis, Data curation, Conceptualization. **Morten Willatzen:** Writing – review & editing, Supervision, Methodology, Conceptualization. **Yogendra Kumar Mishra:** Writing – review & editing, Supervision, Conceptualization. **Zhong Lin Wang:** Writing – review & editing, Supervision.

Declaration of competing interest

The authors declare that they have no known competing financial interests or personal relationships that could have appeared to influence the work reported in this paper.

Data availability

All data are available in the main text or supplementary materials. All other relevant source data are available from the corresponding authors upon reasonable request.

Acknowledgments

None

Funding

This work was supported by the National Key R & D Project from the Minister of Science and Technology (Grant No. 2016YFA0202704), YKM acknowledges the funding by BHH Fonden Denmark, and Fabrikant

Mads Clausen Fond, Denmark.

Supplementary materials

Supplementary material associated with this article can be found, in the online version, at [doi:10.1016/j.mtelec.2024.100102](https://doi.org/10.1016/j.mtelec.2024.100102).

Appendix A. Method

The multiphysics coupled finite element simulation used in this paper is realized by COMSOL software. The calculation involving the piezoelectric properties of ZnO NTs is coupled through structural mechanics and electrostatic fields, and a force or potential is applied as the excitation condition, thereby realizing the simulation of the piezoelectric/inverse piezoelectric effect. Content dealing with the semiconductor properties of ZnO NTs uses structural mechanics, electrostatics, semiconductors, and circuit modules. The calculation process can be described as a two-step approach. Firstly, the piezoelectric potential and carrier concentration under the excitation of external force are calculated, and then the carrier concentration is coupled with the semiconductor module to calculate the carrier transport characteristics of ZnO NTs. Circuits are used to set the source and drain voltages. Details and the parameters utilized in computations can be found in the Supplementary Materials.

References

- [1] X. Wang, J. Zhou, J. Song, J. Liu, N. Xu, Z.L. Wang, Piezoelectric field effect transistor and nanoforce sensor based on a single ZnO nanowire, *Nano Lett.* 6 (2006) 2768–2772, <https://doi.org/10.1021/nl061802g>.
- [2] X. Wang, J. Song, Z.L. Wang, Nanowire and nanobelt arrays of zinc oxide from synthesis to properties and to novel devices, *J. Mater. Chem.* 17 (2007), <https://doi.org/10.1039/b616963p>.
- [3] J.H. He, C.L. Hsin, J. Liu, L.J. Chen, Z.L. Wang, Piezoelectric gated diode of a single ZnO nanowire, *Adv. Mater.* 19 (2007) 781–784, <https://doi.org/10.1002/adma.200601908>.
- [4] Z.L. Wang, Piezopotential gated nanowire devices: piezotronics and piezophotonics, *Nano Today* 5 (2010) 540–552, <https://doi.org/10.1016/j.nantod.2010.10.008>.
- [5] Y. Zhang, Y. Liu, Z.L. Wang, Fundamental theory of piezotronics, *Adv. Mater.* 23 (2011) 3004–3013, <https://doi.org/10.1002/adma.201100906>.
- [6] R. Araneo, G. Lovat, P. Burghignoli, C. Falconi, Piezo-semiconductive quasi-1D nanodevices with or without anti-symmetry, *Adv. Mater.* 24 (2012) 4719–4724, <https://doi.org/10.1002/adma.201104588>.
- [7] L. Guo, S.-T. Han, Y. Zhou, Electromechanical coupling effects for data storage and synaptic devices, *Nano Energy* 77 (2020), <https://doi.org/10.1016/j.nanoen.2020.105156>.
- [8] Z.W. Pan, Z.R. Dai, Z.L. Wang, Nanobelts of semiconducting oxides, *Science* (1979) 291 (2001) 1947–1949, <https://doi.org/10.1126/science.1058120>.
- [9] C.M. Lieber, Z.L. Wang, Functional nanowires, *MRS Bull.* 32 (2007) 99–108, <https://doi.org/10.1557/mrs2007.41>.
- [10] Z.L. Wang, Nanopiezotronics, *Adv. Mater.* 19 (2007) 889–892, <https://doi.org/10.1002/adma.200602918>.
- [11] Z.L. Wang, Towards self-powered nanosystems: from nanogenerators to nanopiezotronics, *Adv. Funct. Mater.* 18 (2008) 3553–3567, <https://doi.org/10.1002/adfm.200800541>.
- [12] Z.L. Wang, ZnO nanowire and nanobelt platform for nanotechnology, *Mater. Sci. Eng. R-Rep.* 64 (2009) 33–71, <https://doi.org/10.1016/j.mser.2009.02.001>.
- [13] Z.L. Wang, Piezotronic and piezophototronic effects, *J. Phys. Chem. Lett.* 1 (2010) 1388–1393, <https://doi.org/10.1021/jz100330j>.
- [14] X.Y. Kong, Y. Ding, R. Yang, Z.L. Wang, Single-crystal nanorings formed by epitaxial self-coiling of polar nanobelts, *Science* (1979) 303 (2004) 1348–1351, <https://doi.org/10.1126/science.1092356>.
- [15] P.X. Gao, Y. Ding, W. Mai, W.L. Hughes, C. Lao, Z.L. Wang, Conversion of zinc oxide nanobelts into superlattice-structured nanohelices, *Science* (1979) 309 (2005) 1700–1704, <https://doi.org/10.1126/science.1116495>.
- [16] Y. Dai, Y. Zhang, Q.K. Li, C.W. Nan, Synthesis and optical properties of tetrapod-like zinc oxide nanorods, *Chem. Phys. Lett.* 358 (2002) 83–86, [https://doi.org/10.1016/S0009-2614\(02\)00582-1](https://doi.org/10.1016/S0009-2614(02)00582-1).
- [17] Z. Wang, J. Qi, S. Lu, P. Li, X. Li, Y. Zhang, Enhancing sensitivity of force sensor based on a ZnO tetrapod by piezo-phototronic effect, *Appl. Phys. Lett.* 103 (2013), <https://doi.org/10.1063/1.4821851>.
- [18] M.C. Newton, P.A. Warburton, ZnO tetrapod nanocrystals, *Mater. Today* 10 (2007) 50–54, [https://doi.org/10.1016/s1369-7021\(07\)70079-2](https://doi.org/10.1016/s1369-7021(07)70079-2).
- [19] Y. Gu, J. Zhou, W. Mai, Y. Dai, G. Bao, Z.L. Wang, Measuring the transport property of ZnO tetrapod using in situ nanoprobe, *Chem. Phys. Lett.* 484 (2010) 96–99, <https://doi.org/10.1016/j.cplett.2009.11.014>.

- [20] Y.K. Mishra, R. Adelung, ZnO tetrapod materials for functional applications, *Mater. Today* 21 (2018) 631–651, <https://doi.org/10.1016/j.mattod.2017.11.003>.
- [21] Z. Zhang, Y. Nan, Y.K. Mishra, M. Willatzen, Z.L. Wang, Understanding the piezoelectric response of ZnO nanotetrapods: detailed numerical calculations, *Appl. Phys. Lett.* 123 (2023), <https://doi.org/10.1063/5.0154454>.
- [22] F. Liu, P.J. Cao, H.R. Zhang, J.Q. Li, H.J. Gao, Controlled self-assembled nanoaeroplanes, nanocombs, and tetrapod-like networks of zinc oxide, *Nanotechnology*. 15 (2004) 949–952, <https://doi.org/10.1088/0957-4484/15/8/013>.
- [23] B.-B. Wang, J.-J. Xie, Q. Yuan, Y.-P. Zhao, Growth mechanism and joint structure of ZnO tetrapods, *J. Phys. D: Appl. Phys.* 41 (2008), <https://doi.org/10.1088/0022-3727/41/10/102005>.
- [24] L. Zanotti, D. Calestani, M. Villani, M. Zha, A. Zappettini, C. Paorici, Vapour-phase growth, purification and large-area deposition of ZnO tetrapod nanostructures, *Cryst. Res. Technol.* 45 (2010) 667–671, <https://doi.org/10.1002/crat.201000081>.
- [25] Y.K. Mishra, S. Kaps, A. Schuchardt, I. Paulowicz, X. Jin, D. Gedamu, S. Freitag, M. Claus, S. Wille, A. Kovalev, S.N. Gorb, R. Adelung, Fabrication of macroscopically flexible and highly porous 3D semiconductor networks from interpenetrating nanostructures by a simple flame transport approach, *Part. Part. Syst. Charact.* 30 (2013) 775–783, <https://doi.org/10.1002/ppsc.201300197>.
- [26] Y.K. Mishra, G. Modi, V. Cretu, V. Postica, O. Lupan, T. Reimer, I. Paulowicz, V. Hrkac, W. Benecke, L. Kienle, R. Adelung, Direct growth of freestanding ZnO tetrapod networks for multifunctional applications in photocatalysis, UV photodetection, and gas sensing, *ACS Appl. Mater. Interfaces*. 7 (2015) 14303–14316, <https://doi.org/10.1021/acsami.5b02816>.
- [27] K. Sun, J. Qi, Q. Zhang, Y. Yang, Y. Zhang, A novel logic switch based on individual ZnO nanotetrapods, *Nanoscale* 3 (2011) 2166–2168, <https://doi.org/10.1039/c1nr10115c>.
- [28] Z. Zhang, L. Sun, Y. Zhao, Z. Liu, D. Liu, L. Cao, B. Zou, W. Zhou, C. Gu, S. Xie, ZnO tetrapods designed as multiterminal sensors to distinguish false responses and increase sensitivity, *Nano Lett.* 8 (2008) 652–655, <https://doi.org/10.1021/nl073088o>.
- [29] M.C. Newton, R. Shaikhaidarov, ZnO tetrapod p-n junction diodes, *Appl. Phys. Lett.* 94 (2009) 153112, <https://doi.org/10.1063/1.3119630>.
- [30] Q. Luo, P. Xu, Y. Qiu, Z. Cheng, X. Chang, H. Fan, Synthesis of ZnO tetrapods for high-performance supercapacitor applications, *Mater. Lett.* 198 (2017) 192–195, <https://doi.org/10.1016/j.matlet.2017.04.032>.
- [31] M. Sharma, M. Poddar, Y. Gupta, S. Nigam, D.K. Avasthi, R. Adelung, R. Abolhassani, J. Fiutowski, M. Joshi, Y.K. Mishra, Solar light assisted degradation of dyes and adsorption of heavy metal ions from water by CuO–ZnO tetrapodal hybrid nanocomposite, *Mater. Today Chem.* 17 (2020), <https://doi.org/10.1016/j.mtchem.2020.100336>.
- [32] V. Postica, J. Gröttrup, R. Adelung, O. Lupan, A.K. Mishra, N.H. de Leeuw, N. Ababii, J.F.C. Carreira, J. Rodrigues, N.B. Sedrine, M.R. Correia, T. Monteiro, V. Sontea, Y.K. Mishra, Multifunctional materials: a case study of the effects of metal doping on ZnO tetrapods with bismuth and tin oxides, *Adv. Funct. Mater.* 27 (2017), <https://doi.org/10.1002/adfm.201604676>.
- [33] D. Gedamu, I. Paulowicz, S. Kaps, O. Lupan, S. Wille, G. Haidarschin, Y.K. Mishra, R. Adelung, Rapid fabrication technique for interpenetrated ZnO nanotetrapod networks for fast UV sensors, *Adv. Mater.* 26 (2014) 1541–1550, <https://doi.org/10.1002/adma.201304363>.
- [34] S. Rackauskas, K. Mustonen, T. Järvinen, M. Mattila, O. Klimova, H. Jiang, O. Tolochko, H. Lipsanen, E.I. Kauppinen, A.G. Nasibulin, Synthesis of ZnO tetrapods for flexible and transparent UV sensors, *Nanotechnology*. 23 (2012) 095502, <https://doi.org/10.1088/0957-4484/23/9/095502>.
- [35] L.A. Ma, T.L. Guo, Morphology control and improved field emission properties of ZnO tetrapod films deposited by electrophoretic deposition, *Ceram. Int.* 39 (2013) 6923–6929, <https://doi.org/10.1016/j.ceramint.2013.02.027>.
- [36] M.C. Newton, S. Firth, P.A. Warburton, ZnO tetrapod Schottky photodiodes, *Appl. Phys. Lett.* 89 (2006) 072104, <https://doi.org/10.1063/1.2335949>.
- [37] Y.-d. Gu, W.-j. Mai, P. Jiang, Characterization of structural and electrical properties of ZnO tetrapods, *Int. J. Min. Met. Mater.* 18 (2011) 686–690, <https://doi.org/10.1007/s12613-011-0497-7>.
- [38] V.A.L. Roy, A.B. Djurišić, H. Liu, X.X. Zhang, Y.H. Leung, M.H. Xie, J. Gao, H.F. Lui, C. Surya, Magnetic properties of Mn doped ZnO tetrapod structures, *Appl. Phys. Lett.* 84 (2004) 756–758, <https://doi.org/10.1063/1.1645312>.
- [39] Y. Liu, S. Niu, Q. Yang, B.D. Klein, Y.S. Zhou, Z.L. Wang, Theoretical study of piezo-phototronic nano-LEDs, *Adv. Mater.* 26 (2014) 7209–7216, <https://doi.org/10.1002/adma.201402328>.
- [40] Y. Liu, Y. Zhang, Q. Yang, S. Niu, Z.L. Wang, Fundamental theories of piezotronics and piezo-phototronics, *Nano Energy* 14 (2015) 257–275, <https://doi.org/10.1016/j.nanoen.2014.11.051>.
- [41] G. Romano, G. Mantini, A. Di Carlo, A. D'Amico, C. Falconi, Z.L. Wang, Piezoelectric potential in vertically aligned nanowires for high output nanogenerators, *Nanotechnology*. 22 (2011) 465401, <https://doi.org/10.1088/0957-4484/22/46/465401>.
- [42] Y. Gao, Z.L. Wang, Electrostatic potential in a bent piezoelectric nanowire: the fundamental theory of nanogenerator and nanopiezotronics, *Nano Lett.* 7 (2007) 2499–2505, <https://doi.org/10.1021/nl071310j>.